

INTEGRATION OF COMPUTATIONAL AND EXPERIMENTAL MODELS FOR DAM-BREAK FLOOD RISK ANALYSIS

M. T. VISEU¹, A. B. ALMEIDA² & A. B. FRANCO²

¹National Laboratory for Civil Engineering, Portugal.

²Department of Civil Engineering, Technical University of Lisbon, Portugal.

ABSTRACT

The knowledge of the maximum water depths associated with dam-break floods is crucial for the population early warning and evacuation plan design, minimizing the losses due to dam failures.

This paper presents an experimental dam-break flood propagation study performed in a physical model and a two-dimensional numerical model suitable to simulate flow propagation on complex topography. First, the numerical model and the physical model of the River Arade valley, located in the south of Portugal (Algarve), are described. A comparison between computed results and measured data is undertaken and uncertainty in the numerical model predictions is analysed.

Keywords: Dam-break, flood wave, physical model, two-dimensional numerical model.

1 INTRODUCTION

Numerical simulation of dam-break flow is a crucial component of risk analysis and dam hazard mitigation, in what concerns the evaluation of flood impact as well as the preparation of valley emergency response in flood prone areas.

In this paper, a physical model representing a real river valley stretch is used to validate a dam-break flood numerical model and to get information related to uncertainties in what concerns the prediction of the hazard (flood) propagation simulation. In fact, for such rare events as dam-break floods, the comparison between the results obtained in a physical model and by a numerical model is one of the best sources of uncertainty characterization.

The physical model represents a reach of the River Arade valley, located in the south of Portugal. Experimental results refer to water depths measured during tests realized for both steady and unsteady flow regimes. The numerical model was developed for the simulation of two-dimensional dam-break flood waves in irregular topography valleys where the one-dimensional approach loses validity, such as in flood plains and where strong variation of the cross section or alignment occurs. It is based on a total variation diminishing (TVD) extension of the two-dimensional MacCormack method and in a scheme to ensure the capacity to simulate flows in domains with general irregular topography.

2 PAST RESEARCH ON PHYSICAL MODELLING OF DAM-BREAK FLOODS

The use of physical models for modelling dam-break flows is not frequent. Dam-break floods routing along a real downstream valley can easily imply physical models with large dimensions or, when choosing a smaller scale to avoid this disadvantage, scale effects can be non-negligible. As a general rule, the use of physical models to study dam-break flood propagation was, in the past, performed after the occurrence of real accidents. For instance, tests in a physical model of Sarrans dam failure, in France, at a scale of 1:300 [1], were done to evaluate the channel roughness influence in the flow configuration of dam-break waves. The failure of Malpasset dam (France) was also studied in a physical model at a scale of 1:400. More recently, the results of this model [2, 3] have been utilized to validate the performance

of some numerical models under the scope of the European Project ‘Concerted Action on Dam Break Modelling (CADAM)’.

Collins [4] presents a description of tests performed in physical models in order to analyse the failure of some German dams – Möhne, Eder and Sorpe – during the Second World War. In Spain, the Tous dam failure [5] has given rise to intense physical modelling tests in order to reproduce the outflow hydrograph. More recently, this dam failure was also chosen as a case study at the IMPACT European Project [6].

The specific use of a physical model to improve the knowledge of some characteristics of dam-break flood propagation is well represented by the physical model of the River Toce. This model studies the flood propagation in a mountain river, emphasizing the role of obstacles as bridges and dwellings localized in the middle of the flow. It reproduces a 5-km reach of the river located in the northern Alps in Italy; the scale of the model is 1:100 and the total area of the experimental facility is $55 \times 13 \text{ m}^2$. Recently, several analyses [7–9] have been performed in order to compare experimental data issued by Toce river physical model with the results of existing one- and two-dimensional numerical models.

3 EXPERIMENTAL STUDIES

3.1 Physical model characteristics

The River Arade is situated in the south-western part of Portugal and has two dams in cascade the Funcho dam and the Silves dam. After this second dam, River Arade spreads along 23 km towards the sea. A 6.0-km reach of the River Arade valley, immediately downstream of the Silves dam, was chosen for the construction of the physical model (Fig. 1).

The physical model is 40-m long and 20-m wide (Fig. 2). It is a non-distorted model at a scale of 1:150 and reproduces a stretch of 6000 m of the river valley [10]. Over the initial 1.7 km, the modelled river is a narrow and straight valley, with one-dimensional flow behaviour. At the end of this stretch, the Baralha Creek tributary enters from the left margin. The following second stretch of the modelled river is 3.7-km long. It is an area where

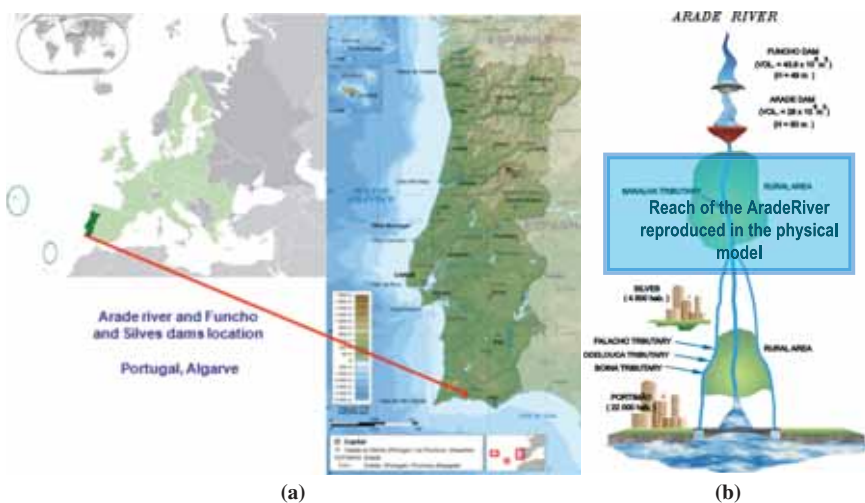


Figure 1: River Arade valley: (a) general location and (b) schematic definition.

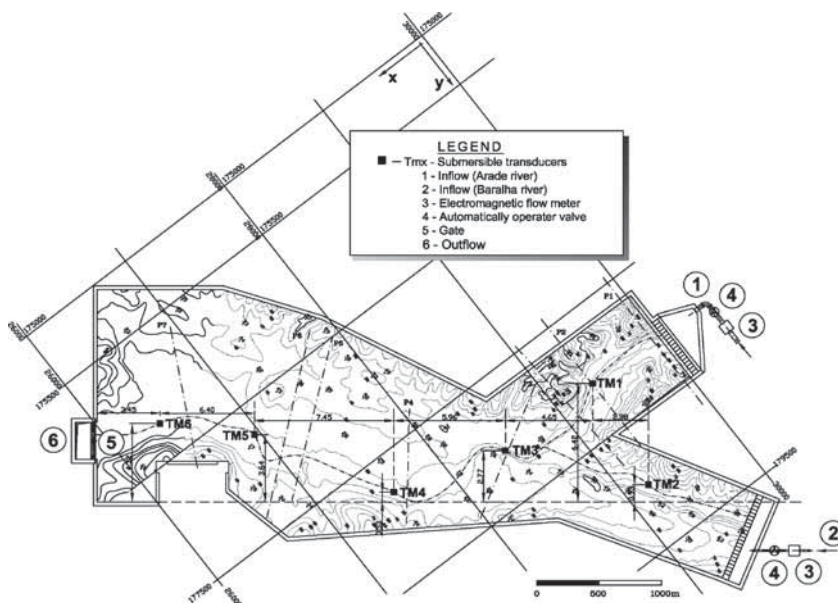


Figure 2: Schematic definition of the River Arade valley physical model.

two-dimensional effects prevail, mainly due to the existence of a wide plain with several singularities such as two consecutive river bends and a narrowing performed by a bridge. Over the final modelled river stretch, the cross-sections narrow again and the flow practically occurs in the x direction; due to this topography, critical flow will occur at the downstream boundary cross-section.

In the physical model, the characteristic ground elevations were materialized through iron curves filled and compacted with clayed sand; the superficial contours were covered by a thick concrete layer painted with water paint.

The installed equipment comprises a system to model and control the flow discharges at the model upstream boundary and a second system to perform the acquisition of water depths along the modelled river valley (Fig. 3).

The discharges are modelled by a closed-loop control system for reproducing the selected flood hydrograph in the upstream boundary of the physical model. The control system comprises an electromagnetic flow meter, an electronic variable speed drive actuating a motorised valve, a computer where the control program (algorithm) runs, as well as an additional hardware unit for interfacing the flow meter and the variable speed drive with the computer [11]. First, a signal profile is saved in the computer, defining the pre-defined flood hydrograph inflowing to the physical model. When the control program is running during an experimental test, it controls the valve motion through the variable speed drive in response to the deviation of the measured output flow comparatively to the specified profile. This closed-loop control system guarantees a significant accuracy in modelling all the desired flood hydrographs.

The discharge can vary between 1.8 l/s, which, in the model, represents the design discharge of the Silves dam spillway (500 m³/s in the prototype), and 100 l/s, which is the maximum discharge allowed by the laboratory installation (27 557 m³/s in the prototype).

A set of 20 rectangular metallic plates are situated on the bottom of the model, each one equipped with submersible transducers (pressure sensors) to measure the time evolution of

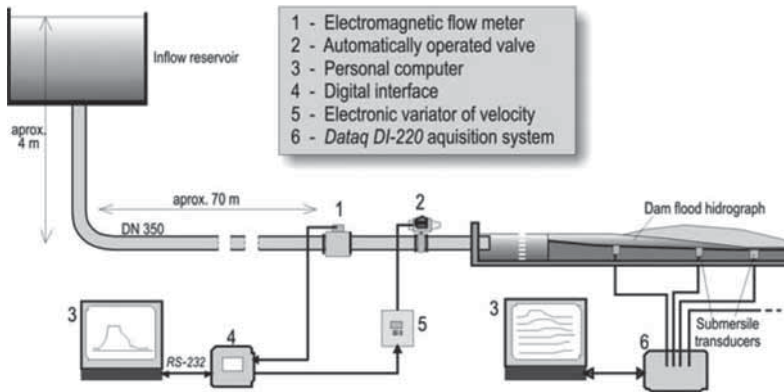


Figure 3: Dam-break flow hydrograph generation and water depth acquisition systems.

water depths. This work presents the recorded data for six of them – transducers T_{m1} through T_{m6} . The placement of these sensors, whose signal is acquired and registered in a second computer, is shown in Fig. 2 and was chosen to illustrate the results of the most important singularities of the model.

3.2 Scale effects

Hydraulic tests involving free surface are usually run according to the Froude similarity law, in the presupposition that the gravity forces are so dominant that surface tension and viscosity forces can just be ignored. Nevertheless, scale effects cannot be avoided in physical models of smaller scales (1:100, 1:150) developed in accordance with the Froude similarity law, due to the fact that Reynolds and Weber numbers are lower in the model than in the prototype; therefore, the influence of the viscosity and surface tensions are higher in the physical model than in nature.

For flows in the turbulent regime, no noticeable scale effects are expected to occur, if the Reynolds number is $>10^4$. Furthermore, laboratory practice [12] shows that the minimum water depth to inhibit scale effects has to be higher than 2 cm.

The expression universally accepted for the Reynolds number is

$$R_e = \frac{vl}{\vartheta} \quad (1)$$

where v is the velocity (mean, local, etc.), l the length (size, depth, diameter, etc.) and ϑ the kinematic viscosity.

A commonly accepted expression for the Reynolds number, R_e , associated with two-dimensional flows, is as follows:

$$R_e = \frac{4Q}{b\vartheta} \quad (2)$$

where Q is the discharge and b the cross-section width.

In what concerns the River Arade valley physical model, the Reynolds number is affected by changes of velocity taking place in space and time and varies with the region of the model because the flow is non-uniform and unsteady. The application of eqn (2), considering

Re equal to 10^4 , to the largest physical model cross section (width equal to 1 km), where surface tension and viscosity forces are more important and therefore can be assumed as the most critical in what concerns this analysis, gives $Q = 5282 \text{ m}^3/\text{s}$. In conclusion, for values of discharges inferior to this last value, scale effects can occur in the largest zones of the model; for larger values of discharge no noticeable scale effects are expected to occur, as gravity forces become dominant and the others stresses can be ignored.

3.3 Tests

The first group of tests was carried out considering several values of discharge and steady flow regime to calibrate the physical model roughness. The estimated value of Strickler coefficient of roughness for the physical model was $Ks_{\text{mod}} = 35 \text{ m}^{1/3}/\text{s}$ (being the Strickler coefficient, Ks , the inverse of the Manning coefficient, n).

The duration of the tests, for both steady and unsteady regimes, had been 15 min. In the steady flow tests, the duration of water depth sampling periods varied between 100 and 200 s with an acquisition frequency of 20 Hz. In the unsteady flow tests, the sampling process had duration of 7.5 min (representing a flood with 1.5 h of duration in the prototype). Preliminary tests showed the adequacy of these values.

3.3.1 Steady flow regime

Eleven tests for steady flow regime were undertaken considering the following values of discharges, scaled up to the prototype [13]:

- i. Discharge value equal to $500 \text{ m}^3/\text{s}$ in the prototype, which is the Silves dam spillway design discharge and
- ii. discharge values equal to 1378, 2756, 8267, 11 023, 13 778, 16 534, 19 290, 22 045, 24 801 and 27 557 m^3/s , in the prototype, which are values corresponding to hypothetical dam-break floods. The measured water depths in the physical model were also scaled up to the prototype. Fig. 5a depicts the time series of water depths, recorded for one value of discharge $Q = 24 801 \text{ m}^3/\text{s}$.

3.3.2 Unsteady flow regime

The unsteady experiments were carried out imposing, in the model upstream boundary, pre-calculated dam-breach discharges hydrographs, according to the most probable failures of Funcho and Silves dams. Four dam-break scenarios (scenarios A–D) have been defined; these descriptions are as follows [14] (i) scenario A: single and total failure of Funcho dam; (ii) scenario B: ‘domino’ failure of both dams, with a total failure of Funcho dam and a partial failure of Silves dam; (iii) scenario C: single and total failure of Silves dam and (iv) scenario D: ‘domino’ and total failures of both dams.

The breach formation process has been simulated using a one-dimensional commercial dam break computational model [15], and the correspondent discharge outflow hydrographs were calculated for all four scenarios (Fig. 4). The worst-case scenario is Scenario D, which presents a maximum discharge, Q_{Max} , equal to $18 090 \text{ m}^3/\text{s}$.

Figure 5b shows, for Scenario D (the total failure of Funcho and Silves dams), the routing of the correspondent outflow hydrograph, i.e. the time evolution of water depth hydrographs measured in the transducers T_{m1} through T_{m6} along the physical model. The measured water depths associated with the other three modelled scenarios are described in detail in [10].

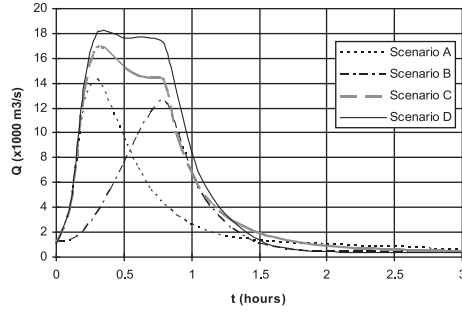


Figure 4: Pre-calculated dam-break flow hydrographs used as upstream boundary conditions for unsteady flow regime tests.

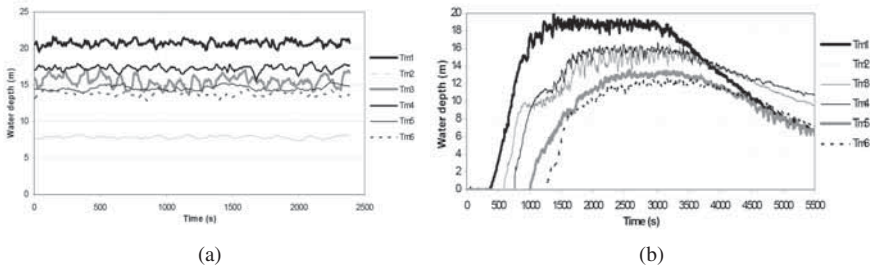


Figure 5: Time series of water depths measured in the physical model: (a) steady flow regime ($Q = 24\,801\text{ m}^3/\text{s}$) and (b) unsteady flow regime tests. Scenario D ($Q_{\text{Max}} = 18\,090\text{ m}^3/\text{s}$).

4 NUMERICAL MODEL

4.1 MacCormack TVD numerical method

The numerical model developed to solve the Saint-Venant equations is based on a TVD extension of the two-dimensional MacCormack method, according to the technique developed by Alcrudo [16, 17] for a two-dimensional finite volume scheme. In the present work, this methodology was adapted to a finite differences scheme, for which the details are described by Franco [18].

In the MacCormack numerical method, the flow variables are calculated for each instant $(n + 1)$ in all the nodes i and j of the computational grid, along the x and y directions, following a predictor/corrector sequence of calculation.

The predictor algorithm (regressive differences) is given by the expression:

$$U_{i,j}^P = U_{i,j}^n - \frac{\Delta t}{\Delta x} (P_{i+1,j}^n - P_{i,j}^n) - \frac{\Delta t}{\Delta y} (R_{i,j+1}^n - R_{i,j}^n) - \Delta t S_{i,j}^n \quad (3)$$

The corrector algorithm (progressive differences) is given by the expression:

$$U_{i,j}^C = U_{i,j}^n - \frac{\Delta t}{\Delta x} (P_{i,j}^P - P_{i-1,j}^P) - \frac{\Delta t}{\Delta y} (R_{i,j}^P - R_{i,j-1}^P) - \Delta t S_{i,j}^P \quad (4)$$

where the superscripts P and C denote the predictor and corrector steps, respectively; U is the vector representing the conservative variables; P and R are the flux vectors in x and y directions; S is the vector representing the topographical and frictional source terms. These vectors are defined as follows:

$$U = \begin{bmatrix} h \\ uh \\ vh \end{bmatrix} \quad P = \begin{bmatrix} uh \\ u^2h + \frac{1}{2}(gh^2) \\ uvh \end{bmatrix} \quad R = \begin{bmatrix} vh \\ uvh \\ v^2h + \frac{1}{2}(gh^2) \end{bmatrix} \quad S = \begin{bmatrix} 0 \\ gh(\Delta Z/\Delta x - J_x) \\ gh(\Delta Z/\Delta y - J_y) \end{bmatrix} \quad (5)$$

where h is the water depth; u and v are the velocity components along the x and y directions; g is the gravitational acceleration; Z is the ground surface elevation; Δx and Δy are the space increment in x and y directions; J_x and J_y are the friction slopes in x and y directions, calculated by the empirical Manning-Strickler formula.

The solution for the next time level step becomes:

$$U_{i,j}^{n+1} = \frac{1}{2}(U_{i,j}^P + U_{i,j}^C) \quad (6)$$

In the presence of abrupt front waves, the solution obtained through the simple MacCormack technique may present spurious oscillations and also shocks without physical consistency because they violate the entropy principle. The TVD methods are capable of rendering the solution oscillation free while retaining second-order accuracy in space and time in the entire computational domain with the exception of the extreme points.

The introduction of the TVD scheme results in the replacement of eqn (6) by

$$U_{i,j}^{n+1} = \frac{1}{2}(U_{i,j}^P + U_{i,j}^C) + \frac{\Delta t}{\Delta x}(D_{i+1/2,j}^n - D_{i-1/2,j}^n) + \frac{\Delta t}{\Delta y}(D_{i,j+1/2}^n - D_{i,j-1/2}^n) \quad (7)$$

The subscripts $i + \frac{1}{2}$, $i - \frac{1}{2}$, $j + \frac{1}{2}$ and $j - \frac{1}{2}$ are intermediate states between grid nodes. The subscript $i + \frac{1}{2}$, for example, denotes the state between (i) and (i + 1). The mathematical expression of the D term is as follows (e.g. for the x direction):

$$D_{i+1/2,j}^n = \frac{1}{2} \sum_{k=1}^3 \alpha_{i+1/2,j}^k \psi(\tilde{a}_{i+1/2,j}^k) \left[1 - \frac{\Delta t}{\Delta x} \left| \tilde{a}_{i+1/2,j}^k \right| \right] \left[1 - \phi(r_{i+1/2,j}^k) \right] \tilde{e}_{i+1/2,j}^k \quad (8)$$

where \tilde{a} and \tilde{e} are the eigenvalues and eigenvectors of the matrix \tilde{A}_j , which is an approximation of the Jacobian matrix of flux A_j . The \tilde{a}^k eigenvalues were defined according to the proposal of Roe [19] and, for the x direction, can be expressed by

$$\tilde{a}^1 = \tilde{u} + \tilde{c} \quad (9)$$

$$\tilde{a}^2 = \tilde{u}$$

$$\tilde{a}^3 = \tilde{u} - \tilde{c}$$

and for the y direction:

$$\tilde{a}^1 = \tilde{v} + \tilde{c} \quad (10)$$

$$\tilde{a}^2 = \tilde{v}$$

$$\tilde{a}^3 = \tilde{v} - \tilde{c}$$

where \tilde{u} , \tilde{v} and \tilde{c} are the Roe averaged variables:

$$\tilde{u} = \frac{u_R \sqrt{h_R} + u_L \sqrt{h_L}}{\sqrt{h_R} + \sqrt{h_L}} \quad (11)$$

$$\tilde{v} = \frac{v_R \sqrt{h_R} + v_L \sqrt{h_L}}{\sqrt{h_R} + \sqrt{h_L}} \quad (12)$$

$$\tilde{c} = \sqrt{\frac{g(h_R - h_L)}{2}} \quad (13)$$

with $R = (i + 1, j)$ and $L = (i, j)$ for the x direction and $R = (i, j + 1)$ and $L = (i, j)$ for the y direction; c is the wave celerity.

For the x direction, the \tilde{e}^k eigenvectors of the approximated matrix \tilde{A}_j are:

$$\tilde{e}^1 = \begin{bmatrix} 1 \\ \tilde{u} + \tilde{c} \\ \tilde{v} \end{bmatrix} \quad \tilde{e}^2 = \begin{bmatrix} 0 \\ 0 \\ \tilde{c} \end{bmatrix} \quad \tilde{e}^3 = \begin{bmatrix} 1 \\ \tilde{u} - \tilde{c} \\ \tilde{v} \end{bmatrix} \quad (14)$$

and for the y direction:

$$\tilde{e}^1 = \begin{bmatrix} 1 \\ \tilde{u} \\ v + \tilde{c} \end{bmatrix} \quad \tilde{e}^2 = \begin{bmatrix} 0 \\ -\tilde{c} \\ 0 \end{bmatrix} \quad \tilde{e}^3 = \begin{bmatrix} 1 \\ \tilde{u} \\ \tilde{v} + \tilde{c} \end{bmatrix} \quad (15)$$

For the x direction, the expressions of $\tilde{\alpha}^k$ which are, in eqn (8), the coefficients of linear combination of the eigenvectors, are:

$$\tilde{\alpha}^{1,3} = \frac{\Delta h}{2} \pm \frac{1}{2\tilde{c}} [\Delta(hu) - \tilde{u} \Delta h] \quad (16)$$

and

$$\tilde{\alpha}^2 = \frac{1}{\tilde{c}} (\Delta(hv) - \tilde{v} \Delta h) \quad (17)$$

In the expressions (15) and (16), $\Delta W = (W_{i+1,j} - W_{i,j})$, considering a suitable variable w and the x direction.

The function $\phi(r_{i+1/2,j}^k)$ is the TVD flux limiter function, used to control the spurious oscillations associated with the second-order schemes. Its purpose, in eqn (8), is to supply artificial dissipation when a discontinuity or strong gradient exists, while adding very little or no dissipation in the regions of smooth variation. In this work, the used limiter is the Van Leer expression [20], which is also based on the \tilde{a}^k eigenvalues of the approximate matrix of flux \tilde{A}_j . For the x direction, the flux limiter coefficient is

$$r_{i+1/2,j}^k = \frac{\tilde{a}_{i+1/2-s,j}^k \left(1 - \left| \frac{\Delta t}{\Delta x} \tilde{a}_{i+1/2-s,j}^k \right| \right) \alpha_{i+1/2-s,j}^k}{\tilde{a}_{i+1/2,j}^k \left(1 - \left| \frac{\Delta t}{\Delta x} \tilde{a}_{i+1/2,j}^k \right| \right) \alpha_{i+1/2,j}^k} \quad (18)$$

with

$$s = \begin{cases} -1 (-) & \text{if } \tilde{a}_{i+1/2,j} < 0 \\ +1 (+) & \text{if } \tilde{a}_{i+1/2,j} > 0 \end{cases} \quad (19)$$

Finally, in eqn (8), the entropy correction factor, Ψ , is introduced in order to avoid a shock occurrence without physical justification. The form adopted in this work is in accordance with Harten and Hyman [21]. The expression is for the x direction:

$$\Psi_{i+1/2,j}^k = \begin{cases} \left| \tilde{a}_{i+1/2,j}^k \right| & \text{if } \left| \tilde{a}_{i+1/2,j}^k \right| \geq \epsilon_{i+1/2,j}^k \\ \epsilon_{i+1/2,j}^k & \text{if } \left| \tilde{a}_{i+1/2,j}^k \right| < \epsilon_{i+1/2,j}^k \end{cases} \quad k = 1, 2 \text{ and } 3 \quad (20)$$

where

$$\epsilon_{i+1/2,j}^k = \max \left[0, (\tilde{a}_{i+1/2,j}^k - a_{i,j}^k), (a_{i,j}^k - \tilde{a}_{i+1/2,j}^k) \right] \quad k = 1, 2 \text{ and } 3 \quad (21)$$

4.2 Modelling the irregular topography

To ensure the capacity of the numerical model to simulate flows in domains with general irregular topography and to recognize possible paths of the flow in each time step, a special treatment imposing internal boundaries conditions was developed. These boundaries, which are temporary and mobile, are generated depending on the water levels values and ground surface elevations in the adjacent computational nodes. Three situations were envisaged where the direct application of the Saint-Venant equations is not permitted and, for each one, additional conditions were defined, in order to determine the intercell fluxes, namely the following: (i) *dry cell*, (ii) *high point* and (iii) *low point*.

In the first situation – *dry cell* – the model sees if there are wet cells in the neighbouring of the grid point (i,j) under calculation, verifying if the water depths in its adjacent grid points are inferior to a value, ϵ , almost equal to 0 (ϵ was considered equal to 10^{-2} m). If this condition occurs, the model imposes flow depth and velocities equal to 0 in grid point (i,j) and the Saint-Venant equations are not applied. The algorithm, for example, in the case of the predictor step with progressive difference in the x direction is

$$\begin{cases} h_{i,j} < \epsilon \\ h_{i+1,j} < \epsilon \\ h_{i,j-1} < \epsilon \end{cases} \quad \text{then } h_{i,j}^p = u_{i,j}^p = v_{i,j}^p = 0 \quad (22)$$

The second situation – *high point* – is guaranteed if the water depth in the grid point (i,j) is 0 and its ground surface elevation $Z(i,j)$ is greater than the water level in the adjacent grid point (Fig. 6).

For example, in the case of the predictor step with regressive differences for the x direction, the model verifies if $h_{i,j}$ and $Z_{i,j} > Z_{i-1,j} + h_{i-1,j}$. If those conditions are guaranteed, the Saint-Venant equations are also not applied and the variables predictions are:

$$h_{i,j}^p = u_{i,j}^p = v_{i,j}^p = 0 \quad (23)$$

The third situation – *low point* – is defined when the water level at the grid point (i,j) is lower than the ground surface elevation at the neighbouring grid point, i.e. in the case of $Z_{i,j} + h_{i,j} < Z_{i+1,j}$ the model generates a reflection boundary following the methodology

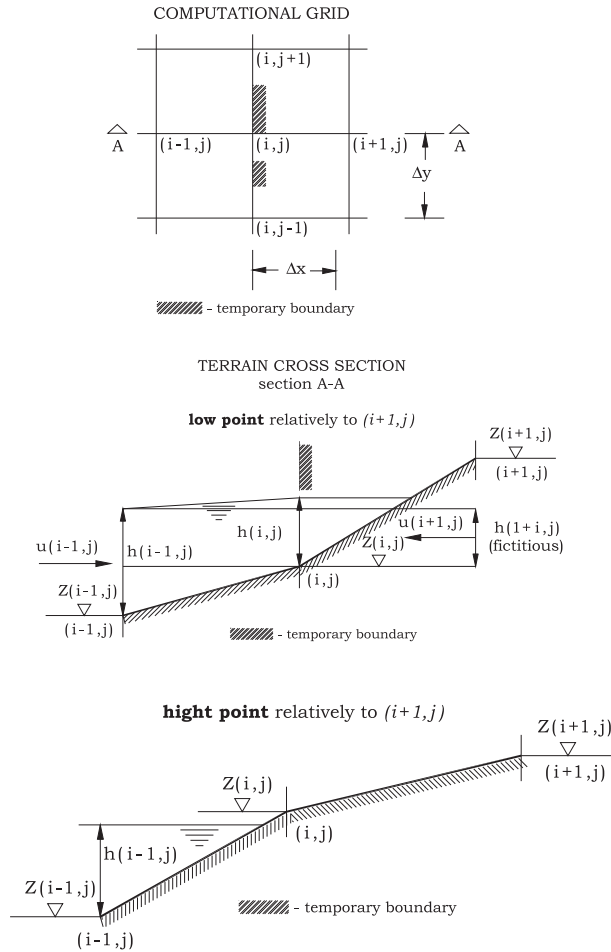


Figure 6: Definition sketch of the internal temporary boundaries.

presented at Fennema and Chaudhry [22] and a fictitious point is created $(i + 1, j)$. In the case of using progressive difference in the x direction (Fig. 6), the following conditions are imposed:

$$Z_{i+1,j} = Z_{i,j} \tag{24}$$

$$h_{i+1,j} = Z_{i-1,j} + h_{i-1,j} - Z_{i,j} \tag{25}$$

$$u_{i+1,j} = -u_{i-1,j} \tag{26}$$

$$v_{i+1,j} = -v_{i-1,j} \tag{27}$$

With these values in the fictitious grid point $(i + 1, j)$, it is possible to apply the MacCormack-TVD method and solve the Saint-Venant equations, obtaining the prediction for the water depth value at grid point (i, j) , $h_{i,j}^p$, and imposing, in the x direction, a null velocity

($u_{i,j}^p = 0,0$). At the end of this computational step, the variable values at grid point $(i + 1,j)$ that have been altered during the previous step are returned to their normal and initial values.

4.3 Model application to river Arade case study

A survey of River Arade valley physical model involving 1500 topographic measurements of the terrain level was performed. As these original data were not suitable for the production of a computational mesh, it was first reduced to a raster grid and then a digital terrain model (DTM) was generated. The DTM includes not only the river valley but also the surrounding system, defining an external boundary with a dimension of $5025 \times 4500 \text{ m}^2$. This area was discretized into an uniform square grid of 202×181 nodes; the spatial steps are $\Delta x = \Delta y = 25 \text{ m}$. The location of each element on the grid system was assigned as well as its ground surface elevation and Strickler roughness coefficient. Figure 7 shows the simulation grid and the points where the water levels were calculated (T_{m1} through T_{m6}), which also correspond to the points where these transducers are located in the physical model.

The numerical simulations were performed with the conditions of the physical model scaling the prototype values. The time interval used is variable and calculated, for each time step, with a maximum Courant number equal to 0.9.

Eleven simulations were performed for steady flow regimes corresponding to hypothetical floods where the maximum discharge value varied between 500 and $27\,557 \text{ m}^3/\text{s}$. Four simulations were performed for unsteady flow regimes corresponding to the chosen dam-break

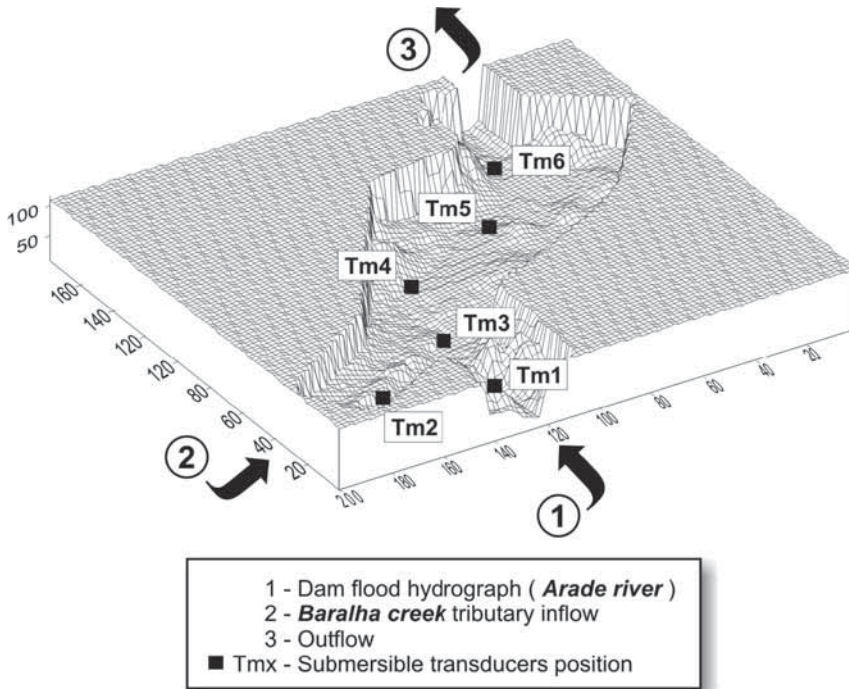


Figure 7: Computational grid for the River Arade valley numerical simulations with submersible transducer positions.

scenarios. For the unsteady flow regime tests, only the computed hydrographs for Scenario D is reported in this paper.

5 RESULTS AND DISCUSSIONS

5.1 Steady flow regime

The comparison of water depths computed with the numerical simulations and measured during steady tests in the six submersible transducers is presented in Fig. 8 (where h is the water depth and Q is the discharge). The analysis of this figure shows that the numerical model reproduces with acceptable accuracy the measured water depths. At transducers T_{m1} , T_{m2} , T_{m4} and T_{m5} , the accuracy of the prediction is significant and differences are felt only for the lower values of the discharge. At transducers T_{m3} and T_{m4} , differences also occur for values of discharge higher than 20 000 m^3/s .

The most noticeable differences appear to be more a consequence of the physical model conditions than to be related to limitations of the numerical model. Therefore, differences between measured and calculated values exist for small values of discharge and are justified by the relative importance of surface tension and viscosity forces when water depths are low. Denote that according to the analysis performed in 3.2, scale effects are expected to occur in

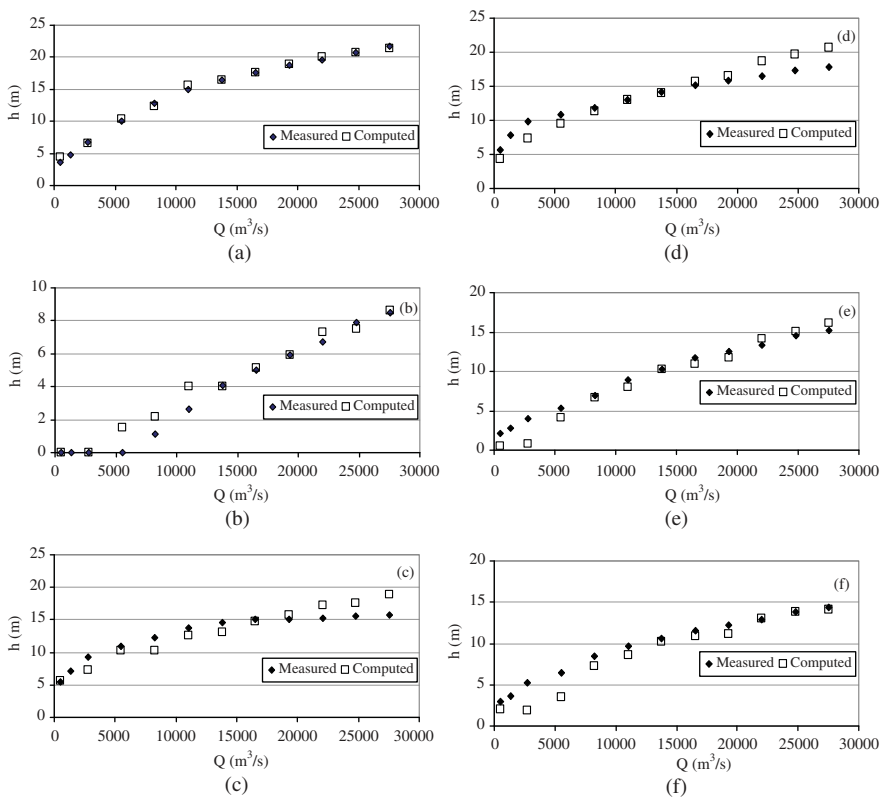


Figure 8: Experimental and computed water depths. Steady flow regime: (a) T_{m1} ; (b) T_{m2} ; (c) T_{m3} ; (d) T_{m4} ; (e) T_{m5} and (f) T_{m6} .

the physical model for values of discharges until 5282 m³/s. Also for transducer T_{m2}, the results denote the influence of scale effects and noticeable differences occur for values of discharge until 11 000 m³/s. This transducer is localized in Baralha Creek tributary and water depths in its location are superior to 2 cm only for discharges above 11 000 m³/s. Therefore, realistic agreement is only reached for higher values of discharges.

At transducers T_{m3} and T_{m4}, substantial agreement with computed water depths is found, except for values of discharge higher than 20 000 m³/s. Those differences can be justified by the transducers positions, just downstream of the confluence of Baralha Creek tributary and after two consecutive bends, in spots where the topography interacts strongly with the flow. In these zones, the water surface measurements showed important oscillations in the tests undertaken for higher discharges values (as presented in the record of the measured water depths in Fig. 5a), leading to higher values of dispersion in relation to a medium value of water depth. For these particular conditions, the differences are rather due to an inaccuracy of the medium water depth to translate all the recorded values of the data set.

The quantification of the uncertainty in the results predicted by the numerical model has been assessed by performing a statistical characterization of the water depths relative errors, e_i, calculated as follows:

$$e_i = \frac{|h_{\text{measured}} - h_{\text{computed}}|}{h_{\text{measured}}} \tag{28}$$

where h_{measured} is the water depth measured in the physical model and h_{computed} the water depth calculated with the numerical model.

Therefore, a sample with 46 values of water depths relative errors was defined and a statistical analysis to judge the accuracy of the numerical model was carried out. The values of water depth obtained for discharge lower than 5282 m³/s were excluded, as scale effects are expected to occur in the physical model for those situations. For the same reason, the errors associated with the first two water depths measured in transducer T_{m2}, localized in the Arade river tributary, were excluded. In fact, those water depths are equal to 1.1 and 2.6 m, which, in the model, respectively represent 0.7 and 1.7 cm, lower than the minimum water depth necessary to inhibit scale effects (2 cm).

Figure 9a shows the empirical cumulative distribution function (CDF) and Fig. 9b the over-time evolution of the water depths relative errors. The second figure shows that water levels' relative errors tend to have an exponential distribution: higher errors decrease very

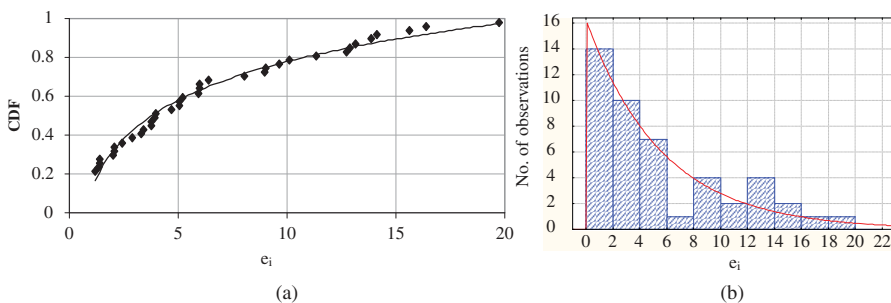


Figure 9: Water depths' relative errors (e_i): (a) cumulative distribution function (CDF) and (b) over-time evolution of the water levels relative errors.

rapidly. According to the empirical distribution, shown in Fig. 9(a), the numerical model presents a probability of almost 60% to estimate water levels with an error inferior to 5%; this latter augments to 80% for a relative error inferior to 10%; there are no errors exceeding 20%.

5.2 Unsteady flow regime

The comparison of water depths' hydrographs concerning the values measured during unsteady tests in the physical model and calculated by the numerical model is presented in Fig. 10 (in this figure h is the water depth and t is the time variable). Only the hydrographs corresponding to Scenario D dam failures are reported.

According to the results depicted in Fig. 10, there are no significant differences between water depths calculated by the numerical model and water levels measured in the physical model. This important statement had already been identified through the results obtained for the steady flow regime tests and simulations. Nevertheless, the analysis of Fig. 10 also shows the existence of discrepancies between numerical and experimental data in what concerns the time of flood arrival and in the attenuation of the falling limb of the hydrographs.

In fact, a general good agreement is observed at transducer T_{m1} , both for water depth and for time of flood arrival. At transducer T_{m2} , apart from some numerical oscillations just after the peak occurrence, the model reproduces the peak flow, the raising limb of the hydrograph and the time of flood arrival reasonably well but fails to reproduce the falling limb of the hydrograph.

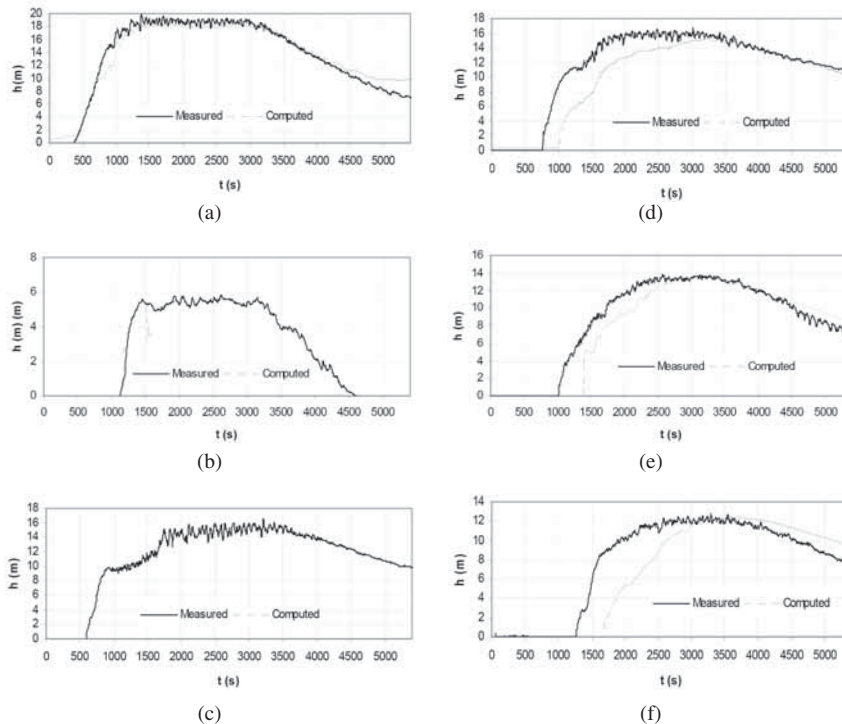


Figure 10: Experimental and computed dam-break water depths. Unsteady flow regime. Scenario D: (a) T_{m1} ; (b) T_{m2} ; (c) T_{m3} ; (d) T_{m4} ; (e) T_{m5} and (f) T_{m6} .

At transducers T_{m3} and T_{m4} , the front wave is slightly more abrupt in the measured hydrographs and the numerical model does slightly smooth the peak flow; this sub-estimation does not seem to have an influence in the downstream flow characteristics; furthermore, the falling limb of the hydrographs is well reproduced but in transducer T_{m4} , located in the flood plain, a small delay of the front wave arrival begins to be perceived.

At transducers T_{m5} and T_{m6} , level measurements are well predicted but numerical times of flood arrival are overestimated; furthermore, the numerical model is able to reproduce the raising limb of the hydrograph, but the numerical falling limb is overestimated.

The results concerning time of flood arrivals confirm that the velocity of the numerical flood wave is smaller than the correspondent to the experimental flood. If there is a good agreement between measured and computed values for the first transducers (T_{m1} and T_{m3}), a slight delay of the numerical flood wave is revealed in the transducer T_{m4} (180 s) and this difference tends to grow as the flood wave travels through the domain of propagation. When it reaches the downstream transducer (T_{m6}), the delay between calculated and observed flood wave is equal to 360 s.

It is also important to notice the similarities and the differences in the shape of the water depths hydrographs. In general, the rising part of these hydrographs is similar for both the computed and the measured values and the front wave is well reproduced. After the peak occurrence, the falling limb decreases slower in the numerical hydrographs than in the measured hydrographs.

These differences seem to be associated rather to the numerical scheme used, as they can also be found in other numerical models using MacCormack-TVD scheme [3, 23], than to the treatment used for modelling the irregular topography. The influence of the bed friction was also investigated and numerical solutions performed adopting higher values for the Strickler coefficient of roughness showed smaller deviations from experimental data in what concerns time of flood arrival (but loosing accuracy in what concerns the water depths).

6 CONCLUSIONS

In this study, a physical model representing a river valley stretch is used to validate a dam-break flood numerical model and to get information related to uncertainties in what concerns the prediction of the characteristics of the flood propagation. The laboratory tests performed jointly with numerical simulations, both for steady and unsteady flow regimes, showed that the dam-break flood routing in a river valley with irregular topography can be similar when a comparison between physical and numerical model results is undertaken.

The numerical model proved to be stable and robust and the systematic comparison performed between its computed data and the measured data in River Arade valley physical model showed that it can accurately reproduce water depths for the tested discharges. Despite the good results, in what concerns water depths, the time of flood arrival calculated with the numerical model is generally higher than the measured in the physical model. This behaviour confirms that the numerical model tends to underestimate the time of flood arrival and this is a conclusion that needs to be considered for safety reasons as regards emergency and evacuation planning.

Finally, the Arade valley physical model proved to be a very important tool in the process of validating the numerical model with respect to dam-break flood routing in natural and irregular valleys, further allowing the assessment of the uncertainty in flood levels prediction by numerical models. This last topic is very important in what concerns the uncertainty characterization related to the valley risk zoning and assessment based on computer simulations.

NOMENCLATURE

The following symbols are used in this paper:

D	TVD term for solution correction in MacCormack TVD numerical scheme
J_x	hydraulic resistance slope in x direction
J_y	hydraulic resistance slope in y direction
$K_{s_{mod}}$	Strickler coefficient of roughness predicted to the River Arade physical model
$K_{s_{num}}$	Strickler coefficient of roughness used to perform numerical simulations
P	flux vector in x direction (Saint-Venant equations)
Q	discharge
Q_{mod}	discharge measured in River Arade physical model
R	flux vector in y direction (Saint-Venant equations)
Re	Reynolds number
S	vector representing the topographical and frictional source terms (Saint-Venant equations)
U	vector representing the conservative variables (Saint-Venant equations)
Z	ground surface elevation
\tilde{a}	eigenvalues of the matrix \tilde{A}_j (approximation of the Jacobian matrix of flux A_j)
\tilde{e}	eigenvectors of the matrix \tilde{A}_j (approximation of the Jacobian matrix of flux A_j)
b	cross section width
c	wave celerity
g	gravitational acceleration
h	water depth
i	space index (x direction)
j	space index (y direction)
q	discharge per unit width
u	velocity component in x direction
r	TVD factor, denoting smoothing capability of the solution in MacCormack TVD numerical scheme
v	velocity component in y direction
α	coefficients of linear combination of the eigenvectors
ϕ	flux limiter function in TVD method
ϑ	kinematic viscosity of water
ψ	entropy correction factor in TVD method
Dy	space increment in y direction
Dt	time increment
Dx	space increment in x direction.

REFERENCES

- [1] Escande, L., Jougaro, F., Castex, L. & Barthet, H. The influence of certain parameters on a sudden flood wave downstream from a dam. *La Houille Blanche*, **5**, pp. 565–575, 1961. doi: <http://dx.doi.org/10.1051/lhb/1961043>
- [2] Hervouet, J.M. & Petitjean, A. Malpasset dam break revisited with two-dimensional computations. *Journal of Hydraulic Research*, **37(6)**, pp. 777–788, 1999. doi: <http://dx.doi.org/10.1080/00221689909498511>
- [3] CADAM. Concerted action on dam break modelling. *Proceedings of the Zaragoza Meeting*, Zaragoza, Spain, European Commission, Brussels, Belgium, November 18–19, 1999-a.

- [4] Collins, A.R., The origins and design of the attack on the German dams. *Proceedings. – The Institution of Civil Engineers, Part 2. Research and Theory*, **73**, pp. 383–405, 1982. doi: <http://dx.doi.org/10.1680/jicep.1982.1707>
- [5] Estrela, T., Hydraulic modelling of the Tous dam break. *Proceedings of the 4th CADAM Meeting*, Spain, November, 1999.
- [6] Impact. Investigation of extreme floods processes and uncertainty. E.C. Research Project reference No. EVG1-CT2001-00037, available at www-impact-project.net, 2001–2004.
- [7] Soares Frazão, S. & Testa, G., Concerted action on dam break modelling. *Proceedings of the 3rd CADAM Meeting – The Toce River Test Case*, Milan, Italy, May, 1999.
- [8] Ying, X. & Wang, S.Y., Modeling flood inundation due to dam and levee breach. *Proceedings of the US-China Workshop on Advanced Computational Modelling in Hydroscience & Engineering*, Oxford, Mississippi, USA, September 19–21, 2005.
- [9] Prestininzi, P., Suitability of the diffusive model for dam-break simulation: application to a CADAM experiment. *Journal of Hydrology*, **361**, pp. 172–185, 2008. doi: <http://dx.doi.org/10.1016/j.jhydrol.2008.07.050>
- [10] Viseu, T., *Dams and Safety of Downstream Valleys. Development of Risk Management Support Methodologies (in Portuguese)*. PhD Thesis, Instituto Superior Técnico, Technical University of Lisbon, Portugal, January, 2006.
- [11] Palma, J.C.P., System for flow control in Arade river physical model (in portuguese). *National Laboratory of Civil Engineering Report n° 315/99*, Lisbon, Portugal, dezembro, 1999.
- [12] Martins, R. & Viseu, T., Estudo em modelo hidráulico do descarregador de cheias da barragem de Abrilongo. *Relatório LNEC*, **331(98)**, pp. 3–4, 1998.
- [13] Viseu, T., Almeida, A.B. & Franco, A.B., River Arade physical model: a tool to validate dam-break flood simulation numerical models. *Proceedings of the 2nd International Symposium Preventing and Fighting Hydrological Disasters*, Timisoara, Romany, July, 2006.
- [14] Viseu, T. & Almeida, A.B., Flood risk assessment in dam's downstream valleys: an approach for safety using numerical and physical models. *Proceedings do 75th Annual Meeting of the ICOLD Symposium Dam Safety Management, Role of State, Private Companies and Public in designing, constructing and operating of large dams*, S. Petersburg, Russia, June, 2007.
- [15] Boss DAMBRK. *User's Manual*, Boss Corporation: Madison, Wisconsin, pp. 6.11–6.25, 1991.
- [16] Alcrudo, F., *Esquemas de Alta Resolución de Variación Total Decreciente para el Estudio de Flujos Discontinuos de Superficie Libre (High Resolution TVD Schemes for Free-Surface Discontinuous Flows)*. PhD Thesis. University of Zaragoza, Spain, 1992.
- [17] Alcrudo, F. & Garcia-Navarro, P., Computing two dimensional flood propagation with a high resolution extension of MacCormack method. *Proceedings of the specialist conference on Modeling of flood propagation over initially dry areas*, Milan, Italy, 3–17, 1994.
- [18] Franco, A.B., *Computational and Experimental Simulation of Flows Induced by Dam-Break (in portuguese)*. PhD Thesis, Instituto Superior Técnico, Technical University of Lisbon, Portugal, 1996.
- [19] Roe, P.L., Approximate Riemann solvers, parameter vectores and difference schemes. *Journal of Computational Physics*, **43**, pp. 357–372, 1981. doi: [http://dx.doi.org/10.1016/0021-9991\(81\)90128-5](http://dx.doi.org/10.1016/0021-9991(81)90128-5)

- [20] Van Leer, B., Towards the ultimate conservative difference scheme, V. A second order sequel to Godunov's method. *Journal of Computational Physics*, **32**, pp. 101–136, 1979. doi: [http://dx.doi.org/10.1016/0021-9991\(79\)90145-1](http://dx.doi.org/10.1016/0021-9991(79)90145-1)
- [21] Harten, A. & Hyman, P., Self-adjusting grid methods for one dimensional hyperbolic conservation laws. *Journal of Computational Physics*, **50**, pp. 235–269, 1983. doi: [http://dx.doi.org/10.1016/0021-9991\(83\)90066-9](http://dx.doi.org/10.1016/0021-9991(83)90066-9)
- [22] Fennema, R.J. & Chaudry, M.H., Explicit methods for 2-D transient free-surface flows. *Journal of Hydraulic Engineering (ASCE)*, **116(8)**, pp. 1013–1034, 1990. doi: [http://dx.doi.org/10.1061/\(ASCE\)0733-9429\(1990\)116:8\(1013\)](http://dx.doi.org/10.1061/(ASCE)0733-9429(1990)116:8(1013))
- [23] CADAM. Concerted action on dam break modelling. *Proceedings of the Milano Meeting*, Enel, Ricerca Polo Idraulico e Strutturale, Milano, Italy, May 6–7, 1999-b.